Using small angle x-ray scattering to examine the aggregation mechanism in silica nanoparticle-based ambigels for improved optical clarity

Glareh N. Kashanchi, Sophia C. King, Susan E. Ju, et al.

View Online   Export Citation   CrossMark

ARTICLES YOU MAY BE INTERESTED IN

AIP Publishing

Using small angle x-ray scattering to examine the aggregation mechanism in silica nanoparticle-based ambigels for improved optical clarity

View Online   Export Citation   CrossMark

Glareh N. Kashanchi,[1] (iD) Sophia C. King,[1] (iD) Susan E. Ju,[1] Ali Dashti,[2] Ricardo Martinez,[2] Yu-Keng Lin,[3] Vivian Wall,[1] Patricia E. McNeil,[3] Michal Marszewski,[2,4] Laurent Pilon,[2,5,6] (iD) and Sarah H. Tolbert[1,3,5,a] (iD)

AFFILIATIONS

[1] Department of Chemistry and Biochemistry, University of California, Los Angeles, Los Angeles, California 90095-1569, USA
[2] Department of Mechanical and Aerospace Engineering, University of California, Los Angeles, Los Angeles, California 90095-1597, USA
[3] Department of Materials Science and Engineering, University of California, Los Angeles, Los Angeles, California 90095-1595, USA
[4] Department of Chemistry and Biochemistry, The University of Toledo, Toledo, Ohio 43606, USA
[5] California NanoSystems Institute, University of California, Los Angeles, Los Angeles, California 90095-8352, USA
[6] Institute of the Environment and Sustainability, University of California, Los Angeles, Los Angeles, California 90095-1496, USA

Note: This paper is part of the JCP Special Topic on Colloidal Gels.
[a] Author to whom correspondence should be addressed: tolbert@chem.ucla.edu. Telephone: +(310) 206-4767

ABSTRACT

Silica-based aerogels are a promising low-cost solution for improving the insulation efficiency of single-pane windows and reducing the energy consumption required for space heating and cooling. Two key material properties required are high porosity and small pore sizes, which lead to low thermal conductivity and high optical transparency, respectively. However, porosity and pore size are generally directly linked, where high porosity materials also have large pore sizes. This is unfavorable as large pores scatter light, resulting in reduced transmittance in the visible regime. In this work, we utilized preformed silica colloids to explore methods for reducing pore size while maintaining high porosity. The use of preformed colloids allows us to isolate the effect of solution conditions on porous gel network formation by eliminating simultaneous nanoparticle growth and aggregation found when using typical sol–gel molecular-based silica precursors. Specifically, we used *in situ* synchrotron-based small-angle x-ray scattering during gel formation to better understand how pH, concentration, and colloid size affect particle aggregation and pore structure. *Ex situ* characterization of dried gels demonstrates that peak pore widths can be reduced from 15 to 13 nm, accompanied by a narrowing of the overall pore size distribution, while maintaining porosities of 70%–80%. Optical transparency is found to increase with decreasing pore sizes while low thermal conductivities ranging from 95 +/− 13 mW/m K are maintained. Mechanical performance was found to depend primarily on effective density and did not show a significant dependence on solution conditions. Overall, our results provide insights into methods to preserve high porosity in nanoparticle-based aerogels while improving optical transparency.

I. INTRODUCTION

In 2015, 51% of the total energy consumed by households in the United States was used to power heating, ventilation, and air conditioning systems.[1] As global temperatures continue to reach new extremes, it is imperative that the insulation performance of building materials be maximized to reduce energy loss through the building envelope, and thus reduce overall building energy consumption. One place where building materials are in need of improvement is windows, which account for ~30% of heat loss from homes.[2] Silica aerogels are a leading candidate as a thermal insulation coating for window applications due to their ability to reach porosities in excess of 90% and thermal conductivities as low as 13 mW/m K.[3,4] However, typical aerogel syntheses involve supercritical drying that results in hazy monoliths due to light scattering by pores exceeding 40 nm in size. In addition, their high porosity and low density reduce their mechanical robustness, limiting their widespread application to windows.[5]

Silica gels are typically synthesized from molecular precursors, often tetraalkoxysilanes or trialkoxyalkylsilanes, which polymerize in solution in three stages.[6–9] First, the monomers initially hydrolyze and condense to form 2–4 nm short-chained oligomers that grow into colloidal nanoparticles. These nanoparticles then aggregate into clusters that eventually form a porous gel network. As the gel ages, neighboring silanol groups at the surface react with each other to form Si–O–Si bonds that strengthen the gel. Once formed, silica gels can be dried by super critical drying to make "aerogels" or by freeze drying to make "cryogels," both resulting in large porosity (>90%) and large pores (>40 nm).[10] Alternatively, ambient pressure drying can be used to prepare "xerogels" by directly drying gels from their as-synthesized pore solvent, resulting in porosities of ≤50%, or after exchanging the pore solvent to a lower surface tension solvent to prepare "ambigels," with porosities of ~70%–85%.[10,11] Overall, the final pore structure that determines the optical properties and thermal conductivity of the gel depends on the rate of particle formation and/or aggregation, which are determined by solution conditions, such as pH, concentration/type of reactants, temperature, and solvent type, as well as the drying method.[12]

Specifically focusing on the reaction pH, there are three different methods of catalysis that can be employed: (1) acid-catalyzed, (2) base-catalyzed, or (3) two-step acid-base catalysis. For all three methods, particle formation occurs from simultaneous hydrolysis and condensation reactions, however, the rate of each reaction is pH dependent. Further challenges arise when trying to understand how pH affects the porous gel network formation because particle growth and aggregation are also occurring concurrently for all three catalysts. In an acid-catalyzed synthesis, hydrolysis occurs faster than condensation and results in a gel made of randomly entangled branched chains with micropores.[13,14] On the other hand, for base-catalyzed syntheses, condensation is more effectively catalyzed, resulting in a gel made of interconnected particles with a wider distribution of larger pores.[13,14] In the two-step acid-base process, precursors are first mixed in an alcohol, water, and acid mixture that favors hydrolysis.[15] Then, the base is added as a second catalyst that increases the rate of condensation and reduces gelling time. Overall, the simultaneous particle growth and aggregation create a complex system where factors like pH dictate pore architecture. As such,

manipulating the gelation process to optimize the final gel structure and produce optically transparent, thermally insulating window coatings is difficult.

An alternative precursor for preparing silica gels that has the potential to offer a higher level of control over feature size is the use of preformed colloidal nanoparticles. Nanoparticle-based gels are a good model system for studying colloidal aggregation because particle growth from molecular-precursors is removed from the gelling process. As a result, an understanding of gel-network formation under reaction-limited vs diffusion-limited aggregation can be developed and extended to molecular-based systems. When utilizing nanoparticles as the building blocks for a gel, network formation is controlled through various colloidal destabilization strategies, such as changing pH or ionic strength, removal of charged ligands, varying the solvent dielectric with co-solvents, or temperature treatments.[16,17]

Nanoparticle-based gels have been prepared from many inorganic materials, such as semiconductors, metals, and metal oxides, for a wide range of applications, such as catalysts, thermal insulators, gas sensors, and optical applications.[18–22] For example, Brock *et al.* synthesized the first nanoparticle-based aerogel made from semiconducting II–VI or IV–VI nanoparticles, such as CdS, for photovoltaic and photosensitizer applications. The surface areas and average pore sizes ranged from 38–250 m^2/g and 5–30 nm, respectively.[23,24] More recently, the Niederberger group prepared a translucent TiO$_2$–Au nanoparticle-based composite aerogel for the photocatalytic reduction of CO$_2$ to methanol.[25] In this case, the highly porous structure allowed for the easy gas flow of CO$_2$ and water vapor, while the large surface area (540–550 m^2/g) maximized contact between the reactants and the photocatalysts. Here, we specifically build on our previous efforts[26–28] where we synthesized silica nanoparticle-based xerogels with relatively low porosities (46%–56%) and small pores (<10 nm) as well as ambigels with higher porosities (70%–81%) and larger pore sizes (14–26 nm) for window insulation applications. Unfortunately, while porosity increased, favorably decreasing thermal conductivity from 104 mW/m K for the xerogels to 80 mW/m K for the ambigels, a reduction in visible transmittance was observed from >90% to 83% due to volumetric light scattering by the increased pore sizes, which is not desirable for a window coating. In this work, we aim to improve these materials by understanding how synthetic parameters affect nanoparticle aggregation to produce monoliths with both high porosity and small pore sizes.

In mesoporous materials, the thermal conductivity is the sum of the contributions from conduction through the solid and gaseous phases and from radiative heat transfer.[29] For the present ambigels, the radiative contribution is negligible due to the small porosity.[30,31] The contribution of gaseous thermal conduction from the air depends on the pore size and the gas pressure. For ambigels, gaseous thermal conduction occurs but is somewhat suppressed because the pore size is smaller than the mean free path of air, which ranges from 63 to 68 nm at 1 atm, depending on the ambient temperature and humidity.[32] Therefore, thermal conductivity for these materials is dominated by the contribution from heat conduction through the solid backbone. The mean free path of heat carriers in the solid phase depends on the material effective density and wall thickness, rather than the size of the pores.[33]

As such, the goal of further reducing pore size without sacrificing porosity is driven by the need for improved optical transparency while maintaining low thermal conductivity. Approaches to reduce pore size while maintaining a high porosity include (1) changing the aggregation mechanism of nanoparticles by fine-tuning solution conditions and (2) using smaller nanoparticles as building blocks for the monolithic slabs.[34–36] In this study, we explore the effect of surface charge, concentration, and particle size on the gelling and aging processes of nanoparticle-based ambigel network formation. The complexity of molecular-based sol–gel chemistry is simplified by using preformed silica nanoparticles in colloidal solutions as the building blocks of monolithic slabs. The gelation and aging processes are studied using *in situ* small-angle x-ray scattering (SAXS) and correlated with the physical properties measured *ex situ* after the monolithic gels are ambiently dried. Such physical properties include porosity and pore size, which, in turn, affect the optical transparency, thermal conductivity, and mechanical performance of the mesoporous monoliths investigated.

II. BACKGROUND

The surface of metal oxide nanoparticles, such as silica in aqueous solutions, is covered with –OH groups that are either deprotonated, protonated, or doubly protonated depending on the pH of the solution.[37] The resulting surface charge attracts counterions in solution to the surface, together creating an electric double layer.[38] As described by Derjaguin, Landau, Verwy, and Overbeek, the so-called DLVO theory of coagulation explains that the stabilization of colloids depends upon the force balance between electrostatic repulsion from the electric double layer at particle surfaces and the van der Waals attraction among adjacent particles.[37,39] As the repulsive forces are reduced by reducing the surface charge – by, for example, reducing the pH – the energy barrier that colliding particles must overcome to stick together decreases and the colloids coagulate.[40] The critical coagulation concentration for colloidal solutions of silica nanoparticles has been found to deviate from predictions based on DVLO theory due to the adsorption of water at the particle surface.[6,34] Indeed, Si–OH groups at the particle surface result in tight hydrogen bonding with water molecules in solution that stabilizes the colloid. Some studies have found, however, that sub-micrometer silica particles do follow DLVO behavior.[41–43] In the present study, we are in the low concentration coagulation regime where the self-assembly of nanoparticles into a gel network is dictated by the balance between repulsive and attractive forces between nanoparticles. As such, by first understanding the nanoparticle aggregation processes, synthetic parameters can be tuned to increase optical transparency by decreasing pore sizes while maintaining a high porosity for low thermal conductivity in our monoliths.

To investigate how changes to surface charge, concentration, and particle size affect the gelling process and porous network formation, we turn to solution phase small angle x-ray scattering (SAXS). Solution SAXS is a powerful method to follow structural change *in situ*, and it is particularly well suited for colloidal systems with low polydispersity, which allows more information to be extracted from the scattering data. The SAXS profiles for colloidal solutions consist of a form factor and a structure factor, which can

be modeled to extract the colloid size/shape and determine particle organization, respectively.[44] One such model is the Unified Scattering Function or Unified fit, which can be applied to complex, hierarchical disordered 3-D structures containing branches and cross-links, known as surface- and mass-fractal structures.[45–47] This model can analyze the combined scattering from multiple levels of related structural features of Guinier and Porod regimes that is typical in a disordered material. The Guinier regime identifies the size of the scattering center that creates scattering intensity, while the Porod regime provides the fractal dimension that describes how branched vs compact the network of scattering centers is.[48,49] Schaefer *et al.* demonstrated the application of the Unified fit to hierarchical aggregates of precipitated silica and pelletized carbon black, where primary particles make up aggregates that then produce agglomerates.[50] In this case, each length scale produced its own scattering level that can be modeled by multiple Unified fits to calculate the size and fractal structure of each level. Such SAXS studies for hierarchical nanoparticle aggregates have also been extended to other metal and metal oxide nanocomposites.[51–53]

III. MATERIALS AND METHODS
A. Materials

Colloidal suspensions of silica nanoparticles in water were obtained from commercial suppliers and used either (1) as received, (2) after concentrating, or (3) after exchanging the counter-ions using ion-exchange resin. The nanoparticles solutions used were Nalco 2326 (d = 10 nm, 15 wt %, NH_4^+ stabilized, Nalco Chemical Company), LiSol[TM] 6 (d = 6 nm, 13–15 wt %, Li^+ stabilized, NYACOL® Nano Technologies, Inc.), and LiSol[TM] 3 (d = 5 nm, 6–8 wt %, Li^+ stabilized, NYACOL® Nano Technologies, Inc.). Amberlite® IRC-120(H) ion exchange resin (Alfa Aesar) was used after preconditioning. The following chemicals were used without further purification: hydrochloric acid (36.5%–38% in water, Certified ACS Plus, Fisher Scientific), heptane (Spectranalyzed[TM], Fisher Scientific), ethanol (200 proof, Rossville Gold Shield), lithium hydroxide (1-hydrate, crystals, Acros Organics), silver nitrate (99.85%, Fisher Scientific), lithium chloride (Fisher Scientific), and Fluorinert FC-70 (SynQuest Laboratories, Inc.).

B. Concentration of nanoparticle solution

To concentrate the commercial colloidal suspensions, 250 ml of a silica nanoparticle solution was poured into a 500 ml round bottom flask and connected to a rotary evaporator at 45 °C with a rotation speed of 200 rpm. The pressure was reduced from 750 to 40 Torr and the solution concentrated to either 50% or 75% the initial volume.

C. Preparation of ion-exchanged nanoparticle solutions

The preparation of the lithium-based ion-exchange resin was adapted from the literature.[54,55] Before exchanging the nanoparticle solutions, the Amberlite® resin was preconditioned with Li^+ ions. To do so, a 200 ml solution of 0.5 M LiOH was prepared by dissolving 419.6 mg $LiOH \cdot H_2O$ in 200 ml water. Then, 72 g of LiCl was dissolved in the LiOH solution. Amberlite® IRC-120(H) resin (100 g) was added and the solution was stirred for 2 h. The pH was adjusted with 0.5 M LiOH solution to match the pH of the

nanoparticle solution to be exchanged before drying via vacuum filtration. The preconditioned resin was thoroughly washed with water to remove trace chloride ions. The washing was complete when the filtrate no longer formed a silver chloride precipitate when an aliquot of 2 wt % $AgNO_3$ solution was added. For ion exchange, a batch process was used where 2 g of preconditioned Amberlite® resin was added to 50 ml of the nanoparticle solution to be exchanged and stirred for 3 h. This process was repeated two additional times by decanting the nanoparticle solution and adding 2 g of fresh, preconditioned Amberlite® resin. Once complete, the exchanged colloidal solution was separated from the resin using vacuum filtration.

D. Transmission electron microscopy

Nanoparticles were loaded onto transmission electron microscopy (TEM) grids by first drying an aliquot of particles in a 20 ml scintillation vial at 80 °C and resuspending them in ethanol using probe-sonication. Then, the carbon-coated grid was dipped into the suspension. Images were collected using a Tecnai G2 TF20 High-Resolution EM, CryoEM, and CryoET (FEI). A TIETZ F415MP 16-megapixel 4kx4k CCD detector and an accelerating voltage of 200 kV were used. ImageJ was used to determine the silica nanoparticle size distribution by manually measuring the diameter of 100 particles.

E. Particle mass fraction measurement

The mass fraction of particles in suspension for each solution, either as received, concentrated, or ion-exchanged, was measured by evaporating 0.5 g of solution in a 20 ml scintillation vial at 80 °C overnight and weighing the dried mass of silica nanoparticles.

F. Ambigel synthesis

The synthesis method used in the present study was adapted from previous literature.[27] Briefly, the pH of each nanoparticle solution was adjusted to the desired value using 2 M HCl. Next, 8 ml of each solution was gently poured over perfluorocarbon (PFC) liquid in a cylindrical Teflon mold and placed in a 25 °C oven to gel and age. The PFC liquid substrate offered a non-stick surface that minimized the adhesion between the gel and the substrate and a smooth surface that minimized surface scattering in the dried gel. The water-filled gel was then transferred to a jar with 50 ml of a

1:1 ethanol:water mixture for solvent exchange. The solvent was exchanged again every 3 h for a total of seven additional exchanges with the following sequence: (1) three times in 50 ml of ethanol, (2) once in 50 ml of a 1:1 ethanol/heptane mixture, and (3) three times in 50 ml of heptane. The heptane-filled gel was then placed in a container and covered with plastic wrap to dry at ambient pressure and temperature. The full list of colloidal solution conditions is presented in Table I.

G. Nitrogen adsorption–desorption porosimetry

All samples were degassed under vacuum at 150 °C for 24 h prior to analysis. The adsorption–desorption isotherms were measured at 77 K using a 3Flex porosimeter equipped with a turbo pump (Micromeritics Instrument Corp., Norcross, GA, USA). Sample porosity (ϕ) was calculated according to[56]

$$\phi = \frac{V_t \rho_s}{(1 + V_t \rho_s)}, \tag{1}$$

where V_t is the total pore volume and ρ_s is the density of bulk silica taken as ρ_s = 2.2 g cm^{-3}.[57] The total pore volume V_t was calculated from the number of moles of nitrogen adsorbed at p/p_0 = 0.98 considering that the molar volume of liquid nitrogen at 77 K is 34.39 cm^3 mol^3.[58] The Brunauer–Emmett–Teller method was used to calculate the specific surface area S_{BET} based on the adsorption data in the relative pressure range p/p_0 = 0.05 to p/p_0 = 0.2 and assuming that the nitrogen molecule cross-sectional area was 0.162 nm^2.[59] The pore size distribution dV_P/dw was calculated from the adsorption branch of the nitrogen isotherm using the Kruk–Jaroniec–Sayari (KJS) method based on the Barrett–Joyner–Halenda (BJH) method.[60,61] For this calculation, statistical film thickness curves were derived from the adsorption branch of the isotherm measured for microporous silica LiChrospher Si-1000 and a modified Kelvin equation calibrated for cylindrical pores up to 19 mm in diameter was used.[60,62] The peak pore diameter, w_p, was estimated as the peak of the obtained pore size distribution and the full width at 5% maximum (FW5%M) was calculated as the difference between the pore diameters that had intensity equal to 5% of the peak pore diameter. Table II summarizes the structural characterization of the pore architecture.

TABLE I. Summary of colloidal solution conditions used for both *in situ* SAXS studies and ambigel synthesis.

Sample	Colloidal solution	Particle size from TEM (nm)	Ion-exchange	Concentration (wt %)	pH
7 nm-pH6-low	LiSol™ 6	7 ± 2	· · ·	16	6
7 nm-pH7-low	LiSol™ 6	7 ± 2	· · ·	16	7
7 nm-pH8-low	LiSol™ 6	7 ± 2	· · ·	16	8
7 nm-pH9-low	LiSol™ 6	7 ± 2	· · ·	16	9
7 nm-pH6-med	LiSol™ 6	7 ± 2	· · ·	24	6
7 nm-pH6-high	LiSol™ 6	7 ± 2	· · ·	32	6
6 nm-pH6-low	LiSol™ 3	6 ± 1	· · ·	16	6
10 nm-pH6-low	Nalco 2326	10 ± 1	$NH_4^+ \rightarrow Li^+$	16	6

TABLE II. Pore structure and optical characterization of dried ambigels. The A after the sample name indicates that the sample is a dried ambigel.

Sample	S_{BET} (m^2/g)	V_t (cm^3/g)	ϕ (%)	w_p (nm)	FW5%M (nm)	L (mm)	T_{vis}^* [a] (%)
7 nm-pH6-low-A	340	1.1	71	15	22	4.15 ± 0.03	82 ± 1
7 nm-pH7-low-A	330	1.1	70	14	15	4.13 ± 0.01	84 ± 0
7 nm-pH8-low-A	340	1.1	70	14	13	4.40 ± 0.02	88 ± 0
7 nm-pH6-med-A	620	1.2	76	14	21	4.74 ± 0.02	82 ± 0
7 nm-pH6-high-A	1010	1.8	80	14	20	5.14 ± 0.02	83 ± 1
6 nm-pH6-low-A	420	1.0	70	13	15	4.17 ± 0.02	85 ± 2
10 nm-pH6-low-A	350	1.2	72	15	22	4.00 ± 0.05	80 ± 2

[a] T_{vis}^* was calculated using optical performance scaled to a thickness of 4.1 mm. T_{vis} calculated without scaling the ambigel thickness is included in the supplementary material.

H. Scanning electron microscopy

A small piece of dried ambigel sample was placed on carbon tape and crushed using a spatula to form a powder. Prior to imaging, all samples were sputtered with gold for 45 s at a pressure of 80 Torr and current of 15 mA using a Hummer® 6.2 sputtering system from Anatech LTD. A model JEOL JSM-6700F field emission electron microscope was used for scanning electron microscopy (SEM) with a 5 kV accelerating voltage and secondary electron detector configuration. High-resolution SEM was performed using a JOEL JSM-IT800SHL Schottky FE-SEM to image polymer templated films with an accelerating voltage of 6 kV.

I. Optical characterization

All samples were heated at 150 °C for 2 h prior to optical measurements to remove physisorbed water. A double-beam Evolution™ 220 Spectrophotometer (Thermo Scientific) equipped with an ISA-220 Integrating Sphere Accessory (5 cm inner diameter, Thermo Scientific) was used. The spectral normal-hemispherical transmittance $T_{nh,\lambda}$ was calculated as

$$T_{nh,\lambda} = \frac{S_{nh,\lambda} - D_{nh,\lambda}}{B_{nh,\lambda} - D_{nh,\lambda}}, \quad (2)$$

where $S_{nh,\lambda}$ is the spectral normal-hemispherical transmitted signal, $D_{nh,\lambda}$ is the dark signal in the absence of light, and $B_{nh,\lambda}$ is the reference normal-hemispherical transmittance measured without a sample. In order to account for thickness variation between ambigels and compare $T_{nh,\lambda}$ with similar photon path lengths, the resulting spectral normal-hemispherical transmittance for all ambigels was scaled to the thickness of 4.1 mm as described in the supplementary material. The thickness-scaled $T_{nh,\lambda}^*$ and non-scaled $T_{nh,\lambda}$ spectral normal-hemispherical transmittance are presented in Fig. 6 and Fig. S1, respectively. Additionally, the visible transmittance T_{vis} was calculated as[63,64]

$$T_{vis} = \frac{\int_{380}^{780} P_\lambda T_\lambda d\lambda}{\int_{380}^{780} P_\lambda d\lambda}, \quad (3)$$

where P_λ is the photopic spectral luminous efficiency function of the human eye.[63] T_{vis}^* results for thickness-scaled spectral normal-hemispherical transmittance are tabulated in Table II and the T_{vis} results for non-scaled spectral normal-hemispherical transmittance are included in Table S1. The thickness dependent optical data used

for the scaling and the optical fit parameters are presented in Fig. S2 and Table S2.

J. Thermal conductivity

The effective thermal conductivity, k_{eff}, of dried monoliths was measured at room temperature in ambient air using a guarded hot plate apparatus operated in a single-sided mode, as described previously.[27,65] Monoliths were initially sanded to ensure a fully flat surface for good thermal contact. The sanding was done by moving an ambigel in a figure eight motion on sandpaper with sequentially increasing grit of P220, P400, P1500, and P2500. The sample thickness ranged between 3.5 and 5.5 mm after sanding and the temperature difference across the sample exceeded 10 °C to minimize the experimental uncertainty, per C177-13 ASTM standard.[66] Each ambigel was placed between a cold and hot plate, which was then set between two blocks of expanded polystyrene and gently compressed for analysis. Multiple layers of insulating cloth were wrapped around the stack to minimize heat loss. The temperature of the cold plate, T_c, was controlled by a chiller circulating water at a constant temperature. The hot plate consisted of two sections, the inner section for measuring thermal conductivity and the outer section for minimizing lateral heat losses. Each section was individually connected to a power supply by resistive wires to independently control currents and Joule heating. Under steady-state conditions based on energy conservation principles and Fourier's law, the effective thermal conductivity k_{eff} was calculated according to

$$k_{eff} = \frac{\dot{Q}_m L}{A_m (T_m - T_c)} = \frac{R_m I_m^2 L}{A_m (T_m - T_c)}, \quad (4)$$

where $\dot{Q}_m$ is the heat generation rate (in W) at steady state and is equal to $R_m I_m^2 L$. Here, R_m is the resistance (in Ω) of the resistive wires, I_m is the supplied current (in A), and A_m is the area of the hot plate inner section. T_m and T_c are the temperatures (in °C) recorded by the thermocouples on the hot and cold sides of the sample, respectively. Measured effective thermal conductivity k_{eff} are plotted in Fig. 9.

Experimental uncertainty arises from systematic error in the measurements of heat flow, surface area, thickness, and temperature.[65,67] Errors in heat flow may result from heat losses through the samples or resistance occurring between the sample and plates. Thickness measurements were completed in triplicate to minimize error in the axial distance between the thermal couples.

Due to cracks in the sample, small error in the surface area coverage was introduced to the measurements even after tightly fittings pieces back together with proper orientation. Uncertainty from the temperature measurements was minimized by first calibrating the thermocouples.

K. Nanoindentation

The nanoindentation tests were performed on an MTS Nano Indenter XP System (MTS Nano Instruments Inc., Oak Ridge, TN, USA) equipped with a Berkovich-type diamond tip. The tip was calibrated using the Oliver-Pharr method.[68] A standard-continuous stiffness measurement at a constant strain rate of 0.05 s^{-1} with a harmonic displacement of 2 nm, frequency of 45 Hz, surface stiffness detection of 50 N/m, and allowable thermal drift of 0.100 nm/s was applied to obtain the hardness and elastic modulus. The effective Poisson's ratio was used as 0.18 and 0.20 for fused and mesoporous silica, respectively.[28,69] The effective hardness H_{eff} and elastic modulus E_{eff} of each indentation were collected by averaging the values from the indentation depths between 1000–1800 nm. The average and associated standard deviation of H_{eff} and E_{eff} were obtained by analyzing all successful indentations from each nanoparticle-based silica ambigel. The results for both H_{eff} and E_{eff} were fit using the power law expressions,[28]

$$(H \text{ or } E)_{eff} = A\rho_{eff}^{B}, \tag{5}$$

where A and B are empirical constants, with B = 2.5–3.8 for silica aerogels.[70] The effective density ρ_{eff} depends on the material porosity φ and density of bulk amorphous silica $\rho_{SiO_2} \approx 2.2$ g cm^{-3} and is defined by $\rho_{eff} = (1 - \varphi)\rho_{SiO_2}$.[71]

L. Small-angle x-ray scattering (SAXS)

SAXS patterns were collected at the Stanford Synchrotron Radiation Lightsource beamline 4–2. Gelation of each original silica nanoparticle colloidal solution was induced by adjusting their pH to 6, 7, 8, or 9 using 2 M HCl. Each solution was then quickly injected into a quartz capillary and loaded into a multicapillary holder equipped with a heating mantle set to 55 °C. SAXS measurements were performed for 8 h with data collection every minute using an x-ray energy of 10 keV, detector distance of 2500 mm, and Dectris Pilatus3 X 1M and Rayonix MX225HE area detectors. Silver behenate was used to calibrate the sample to detector distance, and all 2D sample patterns were reduced to 1D using SAXSPipe. The reduced SAXS patterns were fit using the Unified Fit macro in the Irena package[72] by applying three Guinier-Porod levels.[45,73,74]

The scattering intensity I(q) can be expressed as[45,75]

$$I(q) = Bc(q) + \sum_{i=1}^{3}\left[G_i \exp\left(-\frac{q^2 R_{g_i}^2}{3}\right) \right.$$
$$\left. + B_i \exp\left(-\frac{q^2 R_{g_{i+1}}^2}{3}\right)\left(\frac{1}{q_i^*}\right)^{P_i} \right] S_i(q), \tag{6}$$

where $Bc(q)$ is the instrument background, the index i refers to the scattering level, and B_i and G_i are the intensity terms related to the Guinier and Porod regimes, respectively. Each level i has a unique

Porod exponent P_i and radius of gyration $R_{g,i}$. The Porod exponent P_i is equal to the mass fractal dimension $D_{f,i}$ when $1 \leq P_i \leq 3$, with $P_i = 1$ being the least fractal swollen chains, moving toward Gaussian chains when $P_i = 2$, and finally a clustered network when $P_i = 3$.[76] The radius of gyration $R_{g,i}$ represents the scatterer radius and is defined by the mean-squared distance between the center of mass of the representative scatterer and the geometric center of each constitutive element (e.g., pores). Here, an R_g-cutoff was applied to levels $i = 1, 2$ to treat each level as a distinct population of scatterers that make up the overall observed structure.[72] The diameter d_i of x-ray scatterers at each level was calculated assuming a dense-sphere shape according to

$$d_i = 2\sqrt{\frac{5}{3}}R_{g,i}. \tag{7}$$

Additionally, the data were corrected with a structure factor $S(q)_i$ to account for any correlation in the system resulting from close particle proximity, such that[73,77]

$$S_i(q) = \frac{1}{1 + p_i f(q\eta_i)} \tag{8}$$

and

$$f(q\eta_i) = 3\left(\frac{\sin(q\eta_i) - q\eta_i \cos(q\eta_i)}{q\eta_i^3}\right). \tag{9}$$

Here, p_i corresponds to the degree of correlation ($0 \leq p_i \leq 5.92$) and is equal to eight times the packing efficiency. Therefore, the maximum value of p_i is 5.92 resulting from the packing efficiency of face-centered cubic (FCC) and hexagonal closed pack (HCP) lattices. Finally, η_i represents the average center-to-surface distance between the scatterers such that $\eta_i > R_{g,i}$. The four parameters of most interest in fitting the data are the Porod exponent of the third level D_3 and the radius of gyration $R_{g,i}$ for each level $i = 1, 2, 3$.

IV. RESULTS AND DISCUSSION

To understand the gelling process, we begin by analyzing a single SAXS pattern in detail to understand the type of information that can be extracted. Figure 1 presents a reduced SAXS pattern for a low concentration solution made up of ~7 nm nanoparticles that were aged for 8 h at 55 °C. The three distinct levels are noted by each knee-like curve (Guinier regime) followed by a linear region (Porod regime). Using the Unified fit, $R_{g,i}$ was obtained for each level, which correlates with the size of the structure that contributed to the scattering intensity in that q-range. Here, we retrieved $R_{g,1} = 1.5$ nm, $R_{g,2} = 3.4$ nm, and $R_{g,3} = 15$ nm. Assuming that the networks are made up of dense, spherical particles, the associated diameters of the scatterers are $d_1 = 4$ nm, $d_2 = 8$ nm, and $d_3 = 39$ nm, according to Eq. (7). These diameters suggest that Level 1 (0.15 Å$^{-1} \leq q \leq 0.3$ Å^{-1}) was due to the hairy layer of oligomers (siloxane chains) that are often hypothesized to be anchored to the surface of the gel.[34] Level 2 (0.035 Å$^{-1} \leq q \leq 0.15$ Å^{-1}) corresponds to the nanoparticles themselves while Level 3 (0.005 Å$^{-1} \leq q \leq 0.035$ Å^{-1}) can be attributed to the clusters of particles in the gel network. The similarity between the retrieved value of d_2 and the nanoparticle diameter d is confirmed by the TEM images of the dried suspension shown in Fig. 2(a) where the average measured particle size d was 7 ± 2 nm.
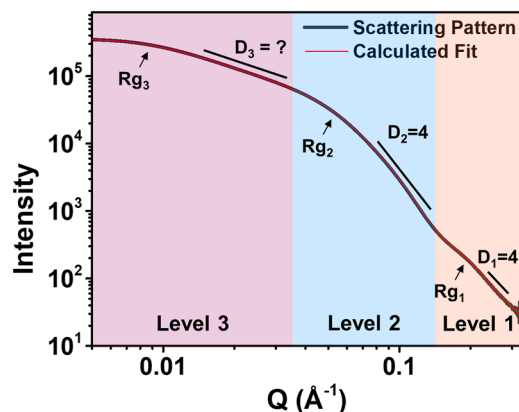
FIG. 1. SAXS pattern from nanoparticle solution with diameter d = 7 nm at pH 7 after 8 h at 55 °C. The three clearly defined levels with the radii of gyration ($R_{g,i}$) and retrieved fractal dimensions ($D_i = -slope$) are delineated by the orange (Level 1), blue (Level 2), and purple (Level 3) regions of the graph.

In the following sections, we discuss experiments where the effects of pH, colloidal concentration, and particle size on the gelling mechanism of colloidal networks were studied. All SAXS patterns were analyzed using the 3-level model described in Fig. 1 to monitor how the pore structure formed and aged. As gelling occurs, the radius of gyration $R_{g,3}$ increases as the individual nanoparticles aggregate to form larger clusters. As the clusters then interact to form the gel network, the fractal dimension D_3 also increases. A plateau in D_3 indicates that gelling of the network is complete and no further aggregation occurs. The final value of D_3 is the mass fractal dimension determined by the complexity of the network. This SAXS information was then compared with *ex situ* characterization of the pore structure for free-standing ambigels prepared from the same nanoparticle solutions.

Nanoparticles solutions containing colloids with a diameter of 7 nm (LiSol^{TM} 6) were first used to study the effect of pH and concentration. Then, to compare the effect of particle size, all nanoparticle solutions (LiSol^{TM} 3, LiSol^{TM} 6, and Nalco 2326) were adjusted to pH 6 and 16 wt %. The summary of synthesis conditions for each sample is listed in Table I. The sample name consists of the particle diameter, pH, and concentration (referred to as low, medium, and high) used for each solution.

To study how the different colloidal solution conditions change optical, thermal insulation, and mechanical properties, ambigels were prepared from all solutions. The porous structure of the ambigels made from solutions 6 nm-pH6-low, 7 nm-pH6-low, and 10 nm-pH6-low are depicted in the SEM images in Figs. 3(a)–3(c). Here, the SEM resolution resolves the clusters of nanoparticles that have randomly aggregated to form the amorphous and porous ambigel. The high resolution SEM image shown in Fig. 3(d) is of a polymer templated film made from the same LiSol^{TM} 3 solution used for the 6 nm-pH6-low sample. This higher resolution resolves the individual sub-10 nm colloids that make up the larger clusters seen in Fig. 3(a), demonstrating that the structure is in fact made up of nanoparticle aggregates.
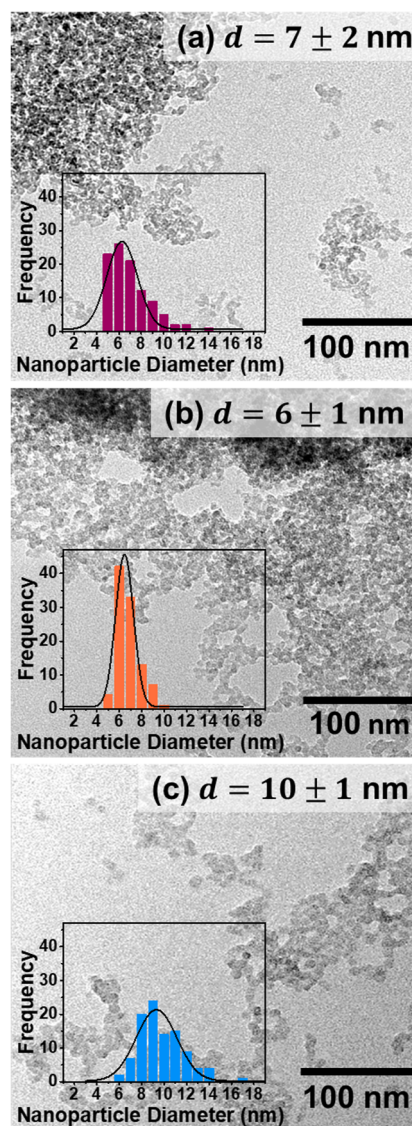

FIG. 2. Transmission electron microscopy (TEM) images with measured nanoparticle size distribution (inset) for the colloidal solutions studied with diameters of (a) $d = 7 \pm 2$ nm, (b) $d = 6 \pm 1$ nm, and (c) $d = 10 \pm 1$ nm.

A. The effect of solution pH

The isoelectric point for silica nanoparticles, i.e., the point of no net electrical charge on the surface, is pH = 2.[78,79] As pH increases from 2, the surface becomes increasingly deprotonated and results in an increased surface charge and greater repulsion from the electric double layer.[79] This increased repulsion is the reason for the high stability of commercial silica colloids in very basic conditions (pH ~ 10). As such, when the pH of commercial colloidal solutions is decreased, the surface charge of the nanoparticles becomes less negative as more –O⁻ groups are protonated. This, in turn, changes the interactions between the repulsive double-layer and attractive dispersion forces that dictate the rate and mechanism of
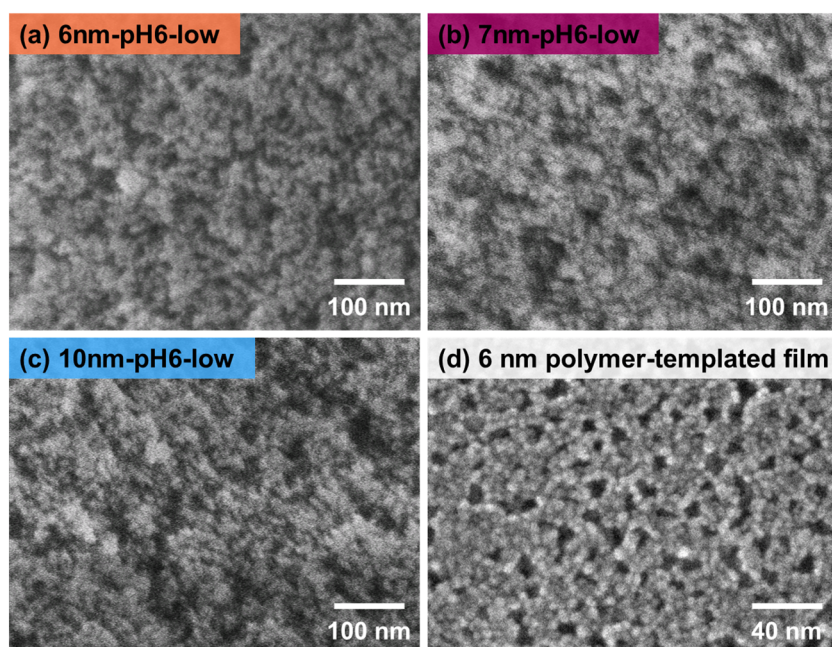
FIG. 3. SEM images of dried ambigels made from low concentration colloidal solutions at pH 6 with particles sizes of (a) 6, (b) 7, and (c) 10 nm. (d) A high resolution SEM image of a polymer templated porous film made with 6 nm nanoparticles resolves the individual particles that make up the larger clusters observed in (a).

gel formation.[34] Easy control over pH, therefore, allows for a systematic tuning of particle aggregation, which determines the pore architecture in the gels.

The time-dependent SAXS patterns of the $d = 7$ nm colloidal solution with pH adjusted to 6, 7, 8, and 9 are shown in Figs. 4(a)–4(d). The 7 nm-pH6-low and 7 nm-pH7-low samples both showed a rapid increase in the Level 3 component compared with 7 nm-pH8-low and 7 nm-pH9-low samples, which showed minimal and no changes, respectively. Specifically, for 7 nm-pH8-low, there was a gradual increase in the Level 3 Porod component. However, the rise was slow and the magnitude of the Level 3 component was sufficiently low that it could not be fit accurately. The solution 7 nm-pH9-low did not show any change in the structure after 8 h, meaning that no significant colloidal aggregation occurred at this high pH over the duration of the experiment. Thus, the data for the 7 nm-pH9-low sample was not analyzed further. Figure 4(e) shows the retrieved fitting parameters for $R_{g,i}$ and D_3 for pH 6, 7, and 8. It indicates that, as expected, $R_{g,1}$ and $R_{g,2}$ remained approximately constant for all pH values, since the same colloidal solution was used, i.e., the layer of siloxane chains and the particle size were unchanged. Focusing on Level 3, the 7 nm-pH6-low and 7 nm-pH7-low samples both showed a gradual rise leading to an eventual plateau in both $R_{g,3}$ and D_3. A plateau was reached in less than 1 h for 7 nm-pH6-low, and trended toward a plateau for 7 nm-pH7-low after 8 h. $R_{g,3}$ and D_3 could not be resolved at t <60 minutes for 7 nm-pH7-low and at no time for 7 nm-pH8-low, indicating limited aggregation in the first hour for 7 nm-pH7-low, and for the first 8 hours for 7 nm-pH8-low. We hypothesize that the onset of the plateau in D_3 marks the time it takes for each solution to form a gel network. The values of $R_{g,3}$ and D_3 in Fig. 4(e) are in agreement with these gelling trends, with smaller cluster sizes and lower fractal dimensions observed in the less reactive pH 7

system. Knoblich and Gerber also observed a decrease in fractal dimension for silica sols in aqueous solutions as pH and gelation time increased due to increased Coulombic repulsion between silica particles and between aggregating clusters.[80,81] The increase in surface charge with increasing pH values hinders aggregation and creates a less fractal, more chain-like network of distanced individual clusters.

Many of the trends with pH can be understood in terms of nanoparticle surface charge density. The nanoparticle surface charge density decreased when the pH was reduced, resulting in less repulsion and more attraction between the nanoparticles. Therefore, as the pH decreased, the number of successful collisions between the nanoparticles and resulting oligomers as they diffused through the solution increased. This resulted in the formation of the gel network and the aggregation could, therefore, be referred to as more "diffusion-limited." On the other hand, since the surface charge density was greater at higher pH, less successful collision events occurred as the particles diffused through solution and the only way to get them to gel was to allow them to sit in an open system where the solvent could evaporate over time; this allowed the distance between the particles to slowly decreased and forced them to interact. This facilitated crosslinking of the reactive –OH groups at the surface of the nanoparticles in an evaporation-driven aggregation mechanism to compensate for the very slow rate of the diffusion-limited process described above.

The increase in $R_{g,3}$ with decreasing pH indicates larger nanoparticle clusters making up the gel network. Since the size of the particles remained relatively unchanged, as noted by the similar $R_{g,2}$ in Fig. 4(e), any differences in the size of the clusters were related to difference in the size of the colloidal clusters and pores throughout the gel. This is demonstrated in Fig. 5(a), which shows the pore size distributions of dried monoliths 7 nm-pH6-low-A, 7
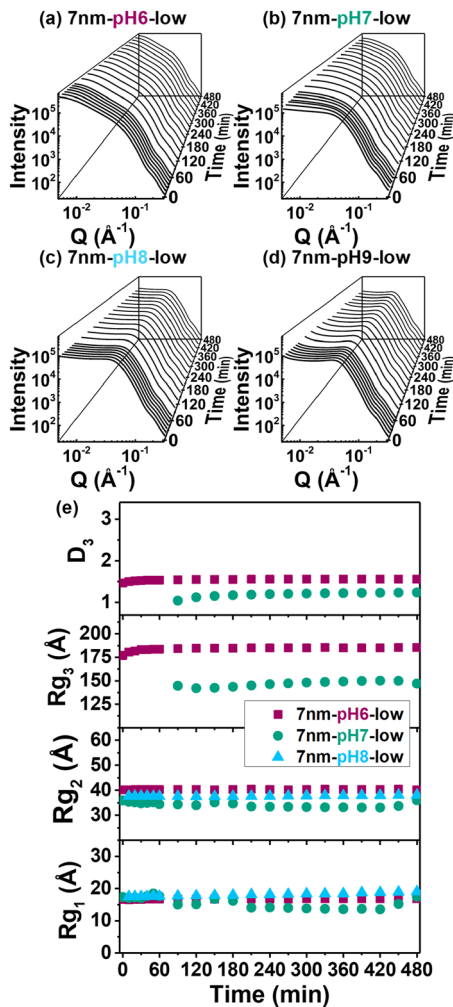
FIG. 4. Structural characterization of 7 nm, low concentration silica nanoparticle solutions gelled at different pH. (a)–(d) Time-resolved x-ray scattering patterns of samples gelled at pH (a) 6, (b) 7, (c) 8, and (d) 9. (e) Fitting parameters for $R_{g,1}$, $R_{g,2}$, $R_{g,3}$ and D_3 obtained from the Unified fit to the SAXS data at pH 6, 7, and 8. Parameters for pH 9 are not included due to a lack of gel network formation.

nm-pH7-low-A, and 7 nm-pH8-low-A. As suggested by the values of $R_{g,3}$ retrieved from the SAXS results of the wet gels, the peak pore diameter increased as the pH decreased. In addition, a significant widening of the pore size distribution can be observed in Fig. 5(b) with increasing full width at 5% max (FW5%M). It is important to note that while pore architecture changed at various pH, the overall porosity of all samples remained relatively constant, as shown in Fig. 5(a) inset. This is significant because reducing pore size is typically paired with a reduction in overall sample porosity. In all solutions, the concentration, and, therefore, the volume of particles present, were identical. However, the resulting packing of particles in the dried monoliths varied due to different aggregation mechanisms.

The reduction in pore sizes with increasing pH gave rise to improved optical properties of the dried monoliths, as evidenced

by the optical images of 7 nm-pH6-low-A, 7 nm-pH7-low-A, and 7 nm-pH8-low-A shown in Figs. 6(a)–6(c). Here, the increased optical clarity is visually observed by the overall reduction in haze, which results from the scattering of light as pH increases. This observation was further quantified by the visible thickness-scaled normal-hemispherical transmittance reported in Fig. 6(h). An increase in $T^*_{nh,\lambda}$ when the pH increases was observed, especially at lower (blue) wavelengths, with T^*_{vis} increasing from 82% to 88%. Therefore, as the pore size decreased throughout the monolith with increasing pH, scattering by individual pores was reduced and the optical clarity increased.[82]

B. The effect of particle concentration

The concentration of Li Sol[TM] 6 was increased from 16 wt % (low) to 24 wt % (medium) and 32 wt % (high) by rotary evaporation and the change in the evolution of the gel and final structure was examined. The SAXS patterns shown in Figs. 7(a)–7(c) demonstrate a quick onset of the Level 3 scattering intensity for all concentrations of nanoparticles, suggesting a rapid gel network formation for all solutions. This is expected as all solutions were prepared at pH 6, which previously demonstrated fast diffusion-limited aggregation. From the data retrieved from the Unified fit in Fig. 7(d), $R_{g,1}$ and $R_{g,2}$ were again approximately the same and constant across all concentrations after all 8 h because all samples were prepared from the same colloidal solution (all the same sized particles) and at the same pH. However, the values diverged in $R_{g,3}$ suggesting a difference in the final gel structure. Examination of Level 3 shows that $R_{g,3}$ of the concentrated solutions (7 nm-pH6-med and 7 nm-pH6-high) plateaued immediately, while a more gradual increase was observed with the original and most dilute solution (low). This suggests that clusters formed immediately for 7 nm-pH6-med and 7 nm-pH6-high while aggregation occurred more slowly for 7 nm-pH6-low. Further, as the concentration increased, the size of $R_{g,3}$ decreased. This decrease in $R_{g,3}$ likely results from the depletion of free particles in solution due to fast aggregation. Instead of a few particle aggregates that grow slowly to a large size at low concentration, high concentration results in simultaneous nucleation and growth of many aggregates, with growth terminated early when the free particle supply is exhausted. Similar to the study performed by Aubert and Cannell, D_3 values for all concentrations at a fixed pH are similar with no systematic trends, suggesting that concentration does not significantly affect fractal dimension.[83]

Figure 5(c) shows the effect of concentration on the pore structure of the dried monoliths. It indicates that the peak pore diameter at 15 nm decreased slightly to 14 nm as the particle concentration increased and that the size distribution shifted toward smaller sizes. Interestingly, increasing concentration for 7 nm-pH6-med-A and 7 nm-pH6-high-A also resulted in greater micropore formation as shown by the second peak in the pore size distribution at ~4 nm. While increasing concentration results in smaller clusters forming, the addition of micropores caused an increase in porosity from 71% to 80%. Photographs for 7 nm-pH6-low-A, 7 nm-pH6-med-A, and 7 nm-pH6-high-A and their thickness-scaled normal-hemispherical transmittance $T^*_{nh,\lambda}$ are presented in Figs. 6(a), 6(d), 6(e), and 6(i), respectively. The introduction of micropores and shift towards smaller pore sizes for
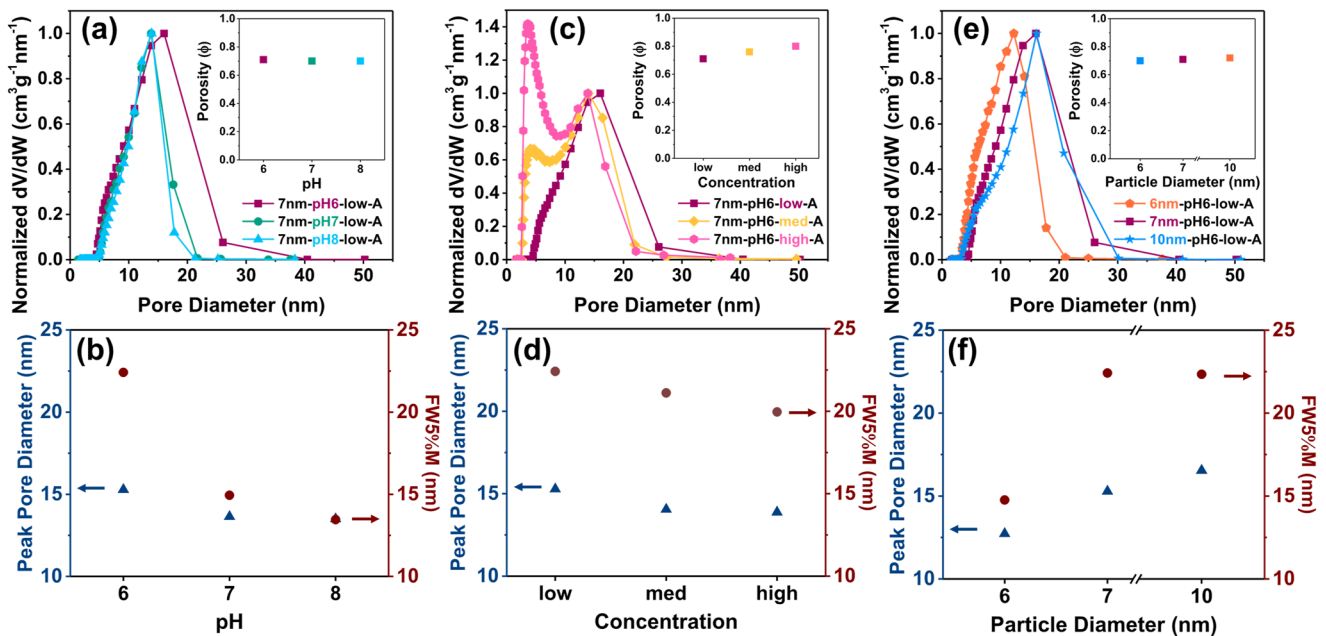
FIG. 5. (a), (c), (e) Pore size distributions and porosities (inset) of dried monolithic slabs measured with N_2 porosimetry at 77 K and (b), (d), (f) the respective peak pore diameter and full width at 5% maximum (FW5%M) demonstrating how (a), (b) pH, (c), (d) concentration, and (e), (f) nanoparticle size change pore structure.
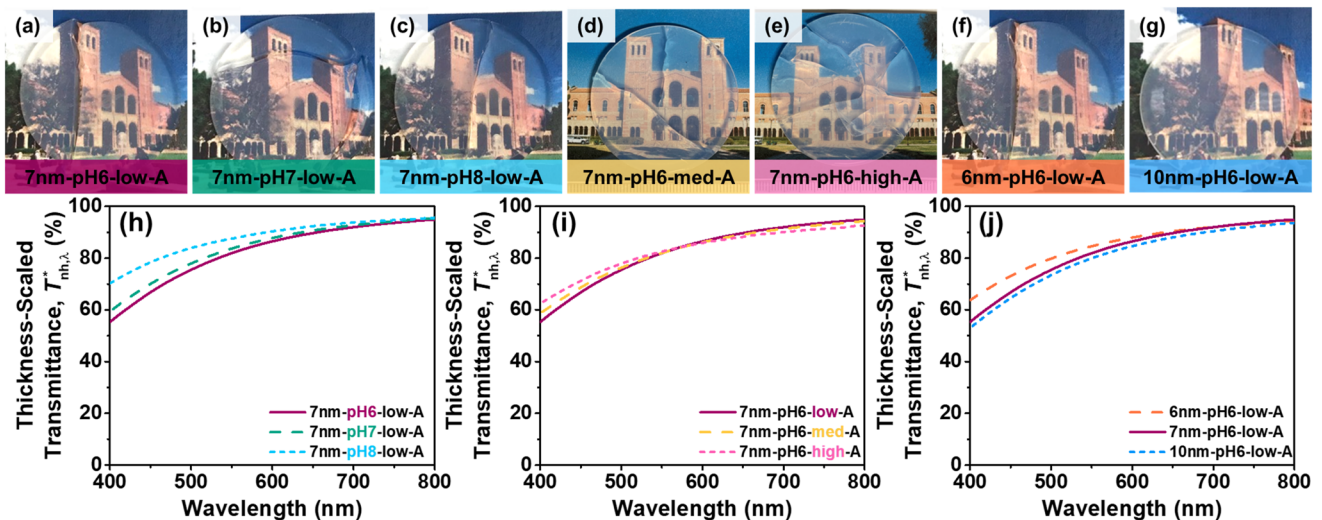

FIG. 6. (a)–(g) Images and (h)–(j) the thickness-scaled spectral normal-hemispherical transmittance $T^*_{nh,\lambda}$ of dried monolithic ambigels demonstrating the effect of (a), (b), (c), (h) pH, (a), (c), (d), (i) concentration, and (a), (f), (g), (j) nanoparticle size on the optical properties. Optical performance for all samples was scaled to a thickness of 4.1 mm as described in the supplementary material.

increasing concentration resulted in an increase of $T^*_{nh,\lambda}$ at lower (blue) wavelengths. However, a slight decrease in $T^*_{nh,\lambda}$ was observed at higher (red) wavelengths. T^*_{vis} for all concentrations remained at 82%–83%.

C. The effect of particle size

Nanoparticle size is a significant parameter as it is directly related to the pore size and porosity as given by Kozeny's equation for a hypothetical porous medium[35]
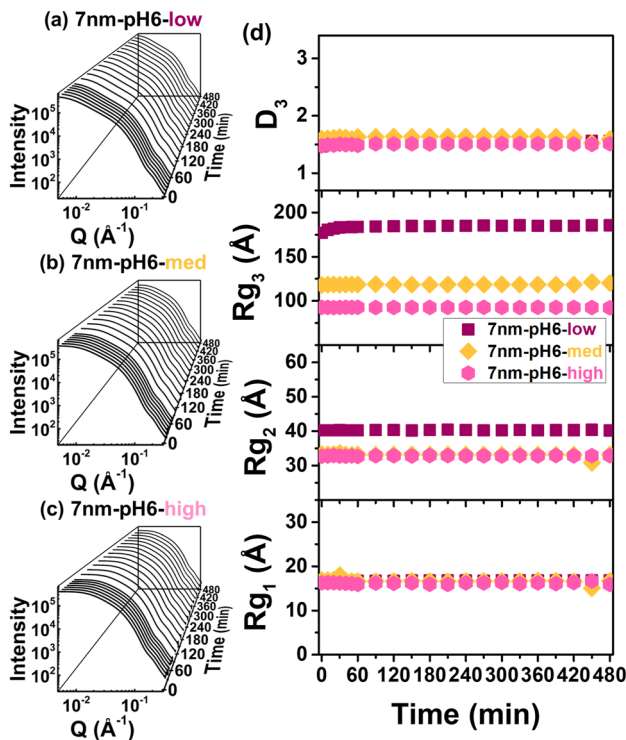
FIG. 7. Structural characterization of 7 nm silica nanoparticle solutions gelled at different concentrations. All samples are at pH 6. (a)–(c) Time-resolved x-ray scattering patterns of samples gelled from (a) low (16 wt %), (b) medium (24 wt %), and (c) high (32 wt %) solutions. (d) Fitting parameters for $R_{g,1}$, $R_{g,2}$, $R_{g,3}$, and D_3 obtained from the Unified fit to the SAXS data at low, medium, and high concentrations.

FIG. 8. Structural characterization of solutions gelled from silica nanoparticle solutions with different particles sizes. All samples are at pH 6 and low concentration. (a)–(c) Time-resolved x-ray scattering patterns of samples gelled from nanoparticle solutions with diameters of (a) 6 nm (b) 7 nm, and (c) 10 nm. (d) Fitting parameters for $R_{g,1}$, $R_{g,2}$, $R_{g,3}$, and D_3 obtained from the Unified fit to the SAXS data of 6, 7, and 10 nm colloidal solutions.

$$\bar{d}_{po} = \frac{2}{3}\left(\frac{\phi}{1-\phi}\right)\bar{d}_{pa} \qquad (10)$$

where $\bar{d}_{po}$ is the average pore diameter, ϕ is porosity, and $\bar{d}_{pa}$ is the average nanoparticle diameter. Equation (10) indicates that, for a fixed porosity, average pore size $\bar{d}_{po}$ decreases with decreasing average particle size $\bar{d}_{pa}$. To explore this phenomenon, the gelation of three nanoparticle solutions with particle diameters of 6, 7, and 10 nm were studied at pH 6 and low concentration. The TEM images and measured particle size distribution of the nanoparticle solutions with diameters of 6, 7, and 10 nm are presented in Fig. 2.

Investigating the structural evolution by SAXS in Figs. 8(a)–8(c), all three solutions present three Levels of scattering intensity. Similar to studying the effect of concentration, this was expected because all solutions were adjusted to pH 6. Looking at the radii of gyration for Levels 1 and 2, the fitted values for $R_{g,1}$ and $R_{g,2}$ shown in Fig. 8(d) show variations across the three samples. As expected. $R_{g,1}$ increased from 1.2 to 1.7 to 3.2 nm and $R_{g,2}$ increased from 3.0 to 4.0 to 4.2 nm for 6 nm-pH6-low, 7 nm-pH6-low, and 10 nm-pH6-low, respectively, reflecting increased radii of gyration with increasing particle diameters. The increase in $R_{g,1}$ resulted from the oligomers on the surface that covered an increasing amount of surface area as size increased,
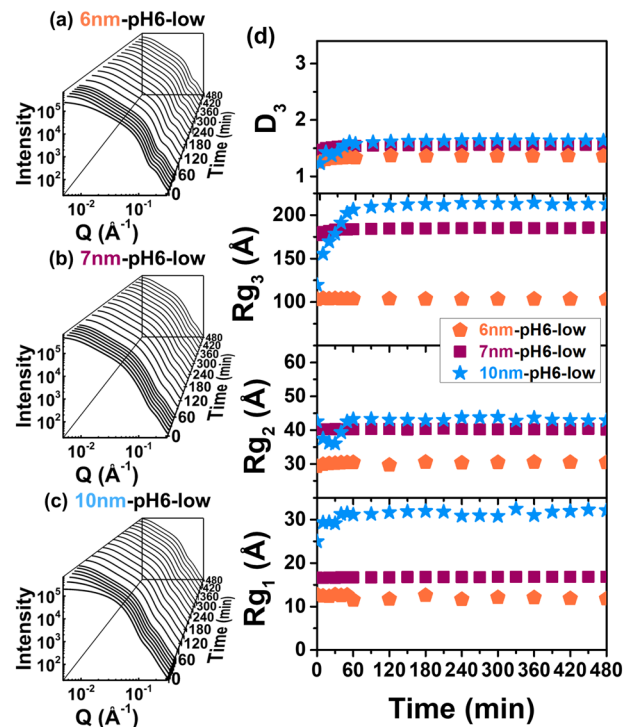
while $R_{g,2}$ increased with particle size because it results from the scattering of the nanoparticles themselves.[34]

Focusing on the cluster size measured by $R_{g,3}$ in Fig. 8(d), the increase in cluster size from 10 nm for the smallest particles (6 nm-pH6-low) to 21 nm for the largest size (10 nm-pH6-low) supports the idea that pore size should increase with particle size at a fixed porosity. As previously mentioned, the size of the Level 3 cluster is related to the pore structure and size throughout the wet gel. In agreement with this idea, Fig. 5(e) and Table II show a pore size increase from 13 nm for 6 nm-pH6-low-A to 15 nm for 10 nm-pH6-low-A at porosities of 70%–72%. We note that the trend is monotonic across all samples; although the measured peak pore width of 7 nm-pH6-low-A and 10 nm-pH6-low-A are similar (~15 nm), the average of the pore size distribution for 7 nm-pH6-low-A is shifted toward smaller pore sizes [Fig. 5(e)], in agreement with the trends for $R_{g,3}$ shown in Fig. 8(d). Additionally, similar to the effect of concentration, D_3 does not change significantly with particle size, suggesting that at pH 6, the diffusion-limited aggregation results in similar fractal structures for all colloids used in this study.

Comparing the thickness-scaled optical transmittance $T^*_{nh,\lambda}$ for these samples in Fig. 6(j), very similar transmittance was obtained for 7 nm-pH6-low-A and 10 nm-pH6-low-A, with a slight increase

for 7 nm-pH6-low-A resulting from the shift in the pore size distribution to smaller pores. For the sample with the smallest sized particles, 6 nm-pH6-low-A, however, the significantly smaller pore sizes gave rise to the highest transmittance at bluer wavelengths because the volumetric scattering was significantly minimized. All pores were smaller than 20 nm and had a negligibly small scattering coefficient for visible wavelengths.[82] The optical properties of these ambigels are observed visually in Figs. 6(a), 6(f), and 6(g).

D. Thermal conductivity

Thus far, this work has demonstrated how the pore architecture of nanoparticle-based gels can be tuned by changing colloidal solution conditions to improve optical transparency of ambigels. For applications like window insulation, high optical transparency is desirable to ensure the quality of a window is not reduced, but that clarity must be combined with high porosity for low thermal conductivity. For all solution conditions, i.e., varying pH, concentration, and nanoparticle size, high porosities of 70%–80% were maintained as shown in Fig. 5 and Table II. The measured effective thermal conductivities for all ambigels as a function of porosity are presented in Fig. 9, which also plots the effective thermal conductivity for other mesoporous silica materials, such as aerogel, ambigels, and thin films prepared from both molecular- and nanoparticle-based precursors.[11,26,27,84–88]

For the samples presented in this work, thermal conductivities ranging from 82 to 108 mW/m K were obtained, which falls in the range for other silica materials with similar porosities. In general, the effective thermal conductivity for materials with porosities ranging from 30% to 60% show a greater dependence on porosity, with effective thermal conductivity decreasing as porosity increases. For 60%–90% porosity, a much smaller dependence of effective
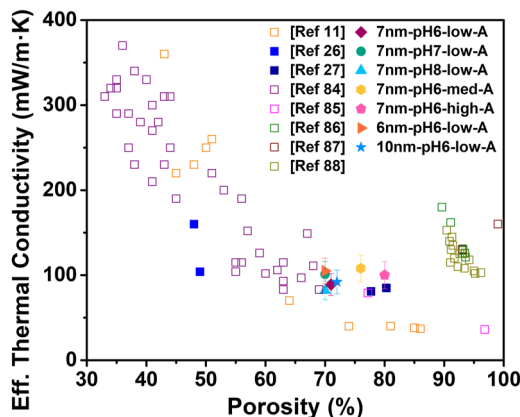
thermal conductivity on porosity is observed. When the porosity of silica aerogels is changed by increasing or decreasing pore size, the thermal conductivity for silica aerogels reaches a minimum at a critical effective density of 120–150 kg/m³.[89–92] Above this effective density when pore sizes decrease, the total thermal conductivity depends strongly on heat conduction through the solid phase, which increases with increasing effective density. Below the critical effective density, the pore sizes within the material may exceed the mean free path of air, resulting in an increase in gaseous thermal conduction and, therefore, in an increase in the total thermal conductivity. We hypothesize that the plateau observed in the effective thermal conductivity measurements for porosities of 70%–80% results from the increasing contribution from heat conduction through the gas phase. The increased gaseous heat conduction compensates for the decrease in the contribution from heat conduction through the solid phase. However, unlike classical silica aerogels with large pore sizes and porosities, the pore sizes of the ambigels in this work are constant. Therefore, the contribution of thermal conduction through the gas phase to the overall effective thermal conductivity remains constant and results in a plateau rather than a minimum. As such, although the porosity for the samples presented here did
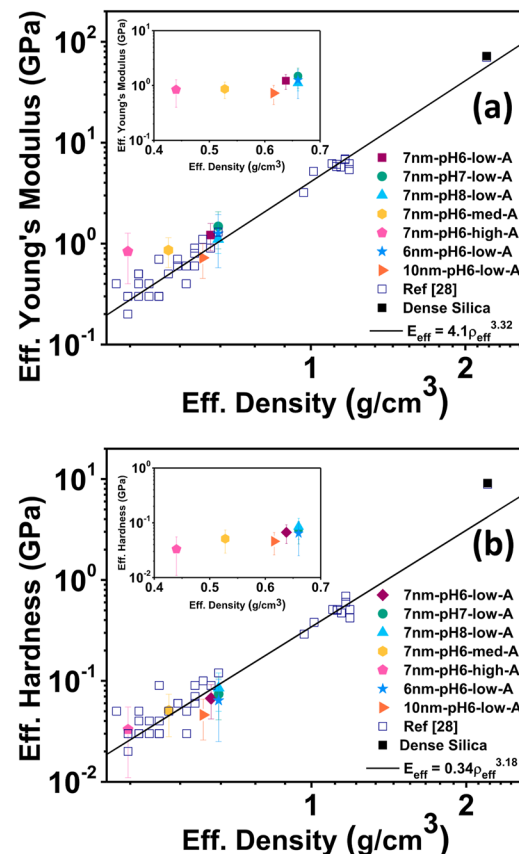

FIG. 9. Effective thermal conductivity as a function of porosity for nanoparticle-based silica ambigels in the present study and reported in literature,[26,27] nanoparticle-based silica thin films,[84] hydrophobic molecular-based silica ambigels,[11,85,88] hydrophobic sodium silicate-based ambigels,[86] and hydrophobic and hydrophilic molecular-based silica aerogels.[87] Filled points indicate nanoparticle-based silica gels prepared by the same synthesis procedure and dried either from water (~50% porosity) or after exchanging the pore solvent to heptane (70%–80% porosity). Thermal conductivity for samples measured in this work and Refs. 11, 26, 27, 84, and 85 were performed at room temperature. References 86–88 do not specify their measurement temperature.

FIG. 10. (a) Effective Young's modulus and (b) effective hardness of nanoparticle-based silica ambigels as a function of effective density. The solid black lines represent power law fits of all nanoparticle-based ambigels given by Eq. (5).

vary slightly, overall a high porosity and small pore sizes were maintained resulting in small changes to the low thermal conductivity measured.

E. Mechanical performance

For any potential applications of these materials, it is important to have an understanding of their mechanical properties. As such, the measured effective Young's modulus and effective hardness as a function of effective density are presented in Fig. 10. In general, the ambigels behave as expected, with effective Young's modulus and effective hardness increasing as effective density increases. Both effective Young's modulus and hardness satisfy power law relationships based on Eq. (5) with respect to the effective density. Changing pH and particle size do not have a significant effect on the mechanical properties, beyond the expected density effect. The one exception is that the Young's modulus of the sample made using high concentration colloidal solution was higher than predicted, suggesting that gel concentration may be a key parameter for modifying the nature and stiffness of the gel network. The hardness showed no significant deviation from the expected density dependence.

V. CONCLUSION

By using preformed silica colloids, we were able to separate gelling from competing hydrolysis and condensation reactions that occur during ambigel synthesis. The effects of pH, concentration, and particle size on the aggregation mechanism and formation of the nanoparticle-based gels were studied using *in situ* small-angle x-ray scattering. The changes each parameter had on the final structure were characterized by measuring porosity, optical transmittance, thermal conductivity, and mechanical performance *ex situ*. We found that increasing the nanoparticle surface charge by increasing the pH of the colloidal solution creates a more reactional-limited aggregation mechanism and slower gel network formation. This, in turn, led to smaller structures in the final ambigel and increased optical clarity. Increasing the particle concentration similarly led to smaller aggregate sizes, which slightly reduced pore size but also resulted in the emergences of micropores that increased the overall porosity. Particle size does correlate directly with both aggregate size during gel formation and pore size after drying when porosity is fixed. Interestingly, although changes in all three parameter affected the ambigel pore structures, adjusting pH was the only solution condition that affected fractal dimension. Finally, thermal conductivities ranging from 82 to 108 mW/m K were maintained and mechanical performance was not significantly affected by solution conditions, but rather depended on the material effective density.

Overall, this work provides insights into methods that can be utilized across various gel syntheses, either molecular- or nanoparticle-based, and applied to aerogel, cryogel, xerogel, and ambigel network formation. The understanding from SAXS on how nanoparticles aggregate to form the wet gel networks under different pH, concentrations, and particle size can guide the choice of conditions for preparing both colloidal and molecular-based gels. In many cases, colloidal precursors form during synthesis in conventional molecular-precursor syntheses. Once a wet gel network has been synthesized with the desired properties, the final pore structure and porosity of the gel will depend on the drying method used, i.e.,

super critical drying (aerogel), freeze drying (cryogel), ambient drying from high surface tension solvents (xerogel), or ambient drying form low surface tension solvents (ambigel). Because this work is focused on optical clarity, smaller pores and lower porosity is desirable, but the same wet gel can result in much higher porosity when super critically dried. Therefore, the drying method should be chosen based on the selected application. For window applications, the ultra-low thermal conductivity resulting from the very high porosity (>90%) of aerogels would be ideal, but the haziness that results from the large pore sizes prevents the use of such highly porous materials. Alternatively, although ambigels have higher thermal conductivity due to their lower porosity, the slight shrinkage that occurs as the solvent evaporates from the material is crucial for reducing the pore size and preparing optically transparent materials better suited for window coatings.

SUPPLEMENTARY MATERIAL

See the supplementary material for non-thickness scaled optical transmittance and details for calculating the thickness-scaled optical transmittance.

AUTHOR DECLARATIONS

Conflict of Interest

The authors have no conflicts to disclose.

Author Contributions

G.N.K. and S. C. K. are contributed equally to this work.

Glareh N. Kashanchi: conceptualization, methodology, formal analysis, data curation, visualization, writing – original draft preparation. **Sophia C. King:** conceptualization, methodology, formal analysis, data curation, visualization, writing – original draft preparation. **Susan E. Ju:** investigation, data curation. **Ali Dashti:** formal

analysis, investigation. **Ricardo Martinez:** formal analysis, investigation, validation. **Yu-Keng Lin:** formal analysis, investigation. **Vivian Wall:** investigation, data curation. **Patricia E. McNeil:** investigation, formal analysis. **Michal Marszewski:** conceptualization, formal analysis, methodology, writing – review & editing. **Laurent Pilon:** conceptualization, supervision, funding acquisition, project administration, writing – review & editing. **Sarah H. Tolbert:** conceptualization, methodology, supervision, funding acquisition, project administration, writing – review & editing.

DATA AVAILABILITY

The data that support the findings of this study are available within the article and its supplementary material. Additional raw data is available upon request of the corresponding author.

REFERENCES

[1] U.S. Energy Information Administration. Table CE3.1 Annual Household Site End-use Consumption in the U.S.—Totals and Averages, 2015; 2018.

[2] See https://www.energy.gov/energysaver/energy-efficient-window-coverings for Energy Efficient Window Coatings; accessed 27 July 2022.

[3] U. Berardi, Energy Procedia **134**, 626 (2017).

[4] N. Hüsing and U. Schubert, Angew. Chem., Int. Ed. **37**, 22 (1998).

[5] T. Shimizu, K. Kanamori, A. Maeno, H. Kaji, C. M. Doherty, P. Falcaro, and K. Nakanishi, Chem. Mater. **28**, 6860 (2016).

[6] R. K. Iler, *The Chemistry of Silica: Solubility, Polymerization, Colloid and Surface Properties and Biochemistry of Silica* (John Wiley and Sons, 1979).

[7] A. Venkateswara Rao, S. D. Bhagat, H. Hirashima, and G. M. Pajonk, J. Colloid Interface Sci. **300**, 279 (2006).

[8] A. Venkateswara Rao, and R. R. Kalesh, Sci. Technol. Adv. Mater. **4**, 509 (2003).

[9] R. Al-Oweini and H. El-Rassy, J. Mol. Struct. **919**, 140 (2009).

[10] A. C. Pierre and G. M. Pajonk, Chem. Rev. **102**, 4243 (2002).

[11] D. M. Butts, P. E. McNeil, M. Marszewski, E. Lan, T. Galy, M. Li, J. S. Kang, D. Ashby, S. King, S. H. Tolbert, Y. Hu, L. Pilon, and B. S. Dunn, MRS Energy Sustainability **7**, 39 (2020).

[12] A. Soleimani Dorcheh and M. H. Abbasi, J. Mater. Process. Technol. **199**, 10 (2008).

[13] F. Koç, S. Sert Çok, and N. Gizli, Res. Eng. Struct. Mater. **6**, 257 (2020).

[14] C. J. Brinker, K. D. Keefer, D. W. Schaefer, and C. S. Ashley, J. Non-Cryst. Solids **48**, 47 (1982).

[15] C. J. Brinker, K. D. Keefer, D. W. Schaefer, R. A. Assink, B. D. Kay, and C. S. Ashley, J. Non-Cryst. Solids **63**, 45 (1984).

[16] C. Ziegler, A. Wolf, W. Liu, A.-K. Herrmann, N. Gaponik, and A. Eychmüller, Angew. Chem., Int. Ed. **56**, 13200 (2017).

[17] F. Matter, A. L. Luna, and M. Niederberger, Nano Today **30**, 100827 (2020).

[18] F. Rechberger and M. Niederberger, Nanoscale Horiz. **2**, 6 (2017).

[19] F. Rechberger, F. J. Heiligtag, M. J. Süess, and M. Niederberger, Angew. Chem., Int. Ed. **53**, 6823 (2014).

[20] F. J. Heiligtag, N. Kränzlin, M. J. Süess, and M. Niederberger, J. Sol-Gel Sci. Technol. **70**, 300 (2014).

[21] T. Berestok, P. Guardia, R. Du, J. B. Portals, M. Colombo, S. Estradé, F. Peiró, S. L. Brock, and A. Cabot, ACS Appl. Mater. Interfaces **10**, 16041 (2018).

[22] N. C. Bigall, A.-K. Herrmann, M. Vogel, M. Rose, P. Simon, W. Carrillo-Cabrera, D. Dorfs, S. Kaskel, N. Gaponik, and A. Eychmüller, Angew. Chem., Int. Ed. **48**, 9731 (2009).

[23] J. L. Mohanan and S. L. Brock, J. Non-Cryst. Solids **350**, 1 (2004).

[24] J. L. Mohanan, I. U. Arachchige, and S. L. Brock, Science **307**, 397 (2005).

[25] F. Rechberger and M. Niederberger, Mater. Horiz. **4**, 1115 (2017).

[26] M. Marszewski, S. C. King, Y. Yan, T. Galy, M. Li, A. Dashti, D. M. Butts, J. S. Kang, P. E. McNeil, E. Lan, B. Dunn, Y. Hu, S. H. Tolbert, and L. Pilon, ACS Appl. Nano Mater. **2**, 4547 (2019).

[27] M. Marszewski, S. C. King, T. Galy, G. N. Kashanchi, A. Dashti, Y. Yan, M. Li, D. M. Butts, P. E. McNeil, E. Lan, B. Dunn, Y. Hu, S. H. Tolbert, and L. Pilon, J. Colloid Interface Sci. **606**, 884 (2022).

[28] M. Marszewski, A. Dashti, P. E. McNeil, M. Fox, V. Wall, D. M. Butts, S. C. King, G. N. Kashanchi, S. H. Tolbert, B. Dunn, and L. Pilon, Microporous Mesoporous Mater. **330**, 111569 (2022).

[29] A. Du, H. Wang, B. Zhou, C. Zhang, X. Wu, Y. Ge, T. Niu, X. Ji, T. Zhang, Z. Zhang, G. Wu, and J. Shen, Chem. Mater. **30**, 6849 (2018).

[30] J.-J. Zhao, Y.-Y. Duan, X.-D. Wang, and B.-X. Wang, J. Non-Cryst. Solids **358**, 1287 (2012).

[31] C. Takai-Yamashita and M. Fuji, Adv. Powder Technol. **31**, 804 (2020).

[32] S. G. Jennings, J. Aerosol Sci. **19**, 159 (1988).

[33] Y. Yan, M. Li, S. King, T. Galy, M. Marszewski, J. S. Kang, L. Pilon, Y. Hu, and S. H. Tolbert, J. Phys. Chem. Lett. **11**, 3731 (2020).

[34] M. Kobayashi, F. Juillerat, P. Galletto, P. Bowen, and M. Borkovec, Langmuir **21**, 5761 (2005).

[35] V. V. Skorokhod, O. I. Get'man, A. E. Zuev, and S. P. Rakitin, Powder Metall. Met. Ceram. **27**, 941 (1988).

[36] T. Galy, D. Mu, M. Marszewski, and L. Pilon, Comput. Mater. Sci. **157**, 156 (2019).

[37] J. C. Brinker and G. W. Scherer, *Sol-Gel Science: The Physics and Chemistry of Sol-Gel Processing* (Academic Press, Inc., 1990).

[38] P. C. Hiemenz and R. Rajagopalan, *Principles of Colloid and Surface Chemistry*, 3rd ed. (Marcel Dekker, Inc., 1997).

[39] E. J. W. Verwey and J. Th. G. Overbeek, *Theory of Stability of Lyophobic Colloids* (Elsevier Publishing Company, Inc., 1948).

[40] G. D. Parfitt, *Dispersion of Powders in Liquids* (Elsevier Applied Science, 1982).

[41] H. Kihira, N. Ryde, and E. Matijević, J. Chem. Soc., Faraday Trans. **88**, 2379 (1992).

[42] R. D. Harding, J. Colloid Interface Sci. **35**, 172 (1971).

[43] S. Barany, M. A. Cohen Stuart, and G. J. Fleer, Colloids Surf., A **106**, 213 (1996).

[44] T. Li, A. J. Senesi, and B. Lee, Chem. Rev. **116**, 11128 (2016).

[45] G. Beaucage, J. Appl. Crystallogr. **29**, 134 (1996).

[46] J. Teixeira, J. Appl. Crystallogr. **21**, 781 (1988).

[47] H. D. Bale and P. W. Schmidt, Phys. Rev. Lett. **53**, 596 (1984).

[48] B. Hammouda, J. Appl. Crystallogr. **43**, 716 (2010).

[49] G. Beaucage, H. K. Kammler, and S. E. Pratsinis, J. Appl. Crystallogr. **37**, 523 (2004).

[50] D. W. Schaefer, T. Rieker, M. Agamalian, J. S. Lin, D. Fischer, S. Sukumaran, C. Chen, G. Beaucage, C. Herd, and J. Ivie, J. Appl. Crystallogr. **33**, 587 (2000).

[51] A.-S. Robbes, J. Jestin, F. Meneau, F. Dalmas, O. Sandre, J. Perez, F. Boué, and F. Cousin, Macromolecules **43**, 5785 (2010).

[52] J. Wang, R. E. Winans, S. L. Anderson, S. Seifert, B. Lee, P. J. Chupas, S. Ren, S. Lee, and Y. Liu, J. Phys. Chem. C **117**, 22627 (2013).

[53] Y.-C. Lin, C.-Y. Chen, H.-L. Chen, T. Hashimoto, S.-A. Chen, and Y.-C. Li, J. Chem. Phys. **142**, 214905 (2015).

[54] H. H. Weldes, Ind. Eng. Chem. Prod. Res. Dev. **9**, 249 (1970).

[55] A. Navarrete-Guijosa, R. Navarrete-Casas, C. Valenzuela-Calahorro, J. D. López-González, and A. García-Rodríguez, J. Colloid Interface Sci. **264**, 60 (2003).

[56] J. Rouquerol, F. Rouquerol, P. Llewellyn, G. Maurin, and K. S. W. Sing, *Adsorption by Powders and Porous Solids: Principles, Methodology, and Applications*, 2nd ed. (Academic Press, Inc., 2013).

[57] R. J. Rumble, *CRC Handbook of Chemistry and Physics*, 98th ed. (CRC Press, Taylor & Francis Group, 2017).

[58] H. Noano, M. Hakuman, and T. Shiono, J. Colloid Interface Sci. **186**, 360 (1997).

[59] M. Kruk and M. Jaroniec, Chem. Mater. **13**, 3169 (2001).

[60] M. Kruk, M. Jaroniec, and A. Sayari, Langmuir **13**, 6267 (1997).

[61] E. P. Barrett, L. G. Joyner, and P. P. Halenda, J. Am. Chem. Soc. **73**, 373 (1951).

[62] M. Jaroniec, M. Kruk, and J. P. Olivier, Langmuir **15**, 5410 (1999).

[63] R. W. G. Hunt, *The Reproduction of Colour*, 6th ed. (John Wiley and Sons, 2004).

[64] NFRC 300-2014, *Test Method for Determining the Solar Optical Properties of Glazing Materials and Systems* (National Fenestration Rating Council, 2013).

[65] A. Ricklefs, A. M. Thiele, G. Falzone, G. Sant, and L. Pilon, Int. J. Heat Mass Transfer **104**, 71 (2017).

[66] ASTM C177-19, *Standard Test Method for Steady-State Heat Flux Measurements and Thermal Transmission Properties by Means of the Guarded-Hot-Plate Apparatus* (ASTM International, 2019).

[67] U. Hammerschmidt, Int. J. Thermophys. **23**, 1551 (2001).

[68] G. M. Pharr and W. C. Oliver, MRS Bull. **17**, 28 (1992).

[69] S. P. Patil, A. Rege, M. Itskov, and B. Markert, J. Phys. Chem. B **121**, 5660 (2017).

[70] H.-S. Ma, A. P. Roberts, J.-H. Prévost, R. Jullien, and G. W. Scherer, J. Non-Cryst. Solids **277**, 127 (2000).

[71] *CRC Handbook of Chemistry and Physics*, 98th ed., edited by J. R. Rumble (CRC Press, Taylor & Francis Group, New York, 2017).

[72] J. Ilavsky and P. R. Jemian, J. Appl. Crystallogr. **42**, 347 (2009).

[73] G. Beaucage, T. A. Ulibarri, E. P. Black, and D. W. Schaefer, ACS Symp. Ser. **585**, 97 (1995).

[74] G. Beaucage, S. Rane, S. Sukumaran, M. M. Satkowski, L. A. Schechtman, and Y. Doi, Macromolecules **30**, 4158 (1997).

[75] G. Beaucage, J. Appl. Crystallogr. **28**, 717 (1995).

[76] G. C. Bushell, Y. D. Yan, D. Woodfield, J. Raper, and R. Amal, Adv. Colloid Interface Sci. **95**, 1 (2002).

[77] A. McGlasson, K. Rishi, G. Beaucage, M. Chauby, V. Kuppa, J. Ilavsky, and M. Rackaitis, Macromolecules **53**, 2235 (2020).

[78] M. L. Fisher, M. Colic, M. P. Rao, and F. F. Lange, J. Am. Ceram. Soc. **84**, 713 (2001).

[79] J. A. A. Júnior and J. B. Baldo, New J. Glass Ceram. **4**, 29 (2014).

[80] B. Knoblich and T. Gerber, J. Non-Cryst. Solids **283**, 109 (2001).

[81] B. Knoblich and T. Gerber, J. Non-Cryst. Solids **296**, 81 (2001).

[82] M. Rubin and C. M. Lampert, Sol. Energy Mater. **7**, 393 (1983).

[83] C. Aubert and D. S. Cannell, Phys. Rev. Lett. **56**, 738 (1986).

[84] Y. Yan, S. C. King, M. Li, T. Galy, M. Marszewski, J. S. Kang, L. Pilon, Y. Hu, and S. H. Tolbert, J. Phys. Chem. C **123**, 21721 (2019).

[85] T.-Y. Wei, T.-F. Chang, S.-Y. Lu, and Y.-C. Chang, J. Am. Ceram. Soc. **90**, 2003 (2007).

[86] U. K. H. Bangi, I.-K. Jung, C.-S. Park, S. Baek, and H.-H. Park, Solid State Sci. **18**, 50 (2013).

[87] A. Alperen Günay, H. Kim, N. Nagarajan, M. Lopez, R. Kantharaj, A. Alsaati, A. Marconnet, A. Lenert, and N. Miljkovic, ACS Appl. Mater. Interfaces **10**, 12603 (2018).

[88] A. P. Rao, G. M. Pajonk, and A. V. Rao, J. Mater. Sci. **40**, 3481 (2005).

[89] J.-J. Y.-Y. Duan, X.-D. Wang, and B.-X. Wang, J. Phys. D: Appl. Phys. **46**, 015304 (2013).

[90] X. Lu, R. Caps, J. Fricke, C. T. Alviso, and R. W. Pekala, J. Non-Cryst. Solids **188**, 226 (1995).

[91] G. Wei, Y. Liu, X. Zhang, F. Yu, and X. Du, Int. J. Heat Mass Transfer **54**, 2355 (2011).

[92] J. Fricke and T. Tillotson, Thin Solid Films **297**, 212 (1997).